Formation of lenticular sedimentary structures

Abstract *(up to 300 words)*
A numerical model that computes the vertical distribution of different sediment sizes in riverbeds has been used to predict the formation of lenticular sedimentary structures. The numerical model solved the Navier-Stokes equations to find the water velocities and the turbulence. Convection-diffusion equations were used to predict the sediment concentrations. Algorithms for changes in the elevations of water surface and bed due to erosion and deposition were also included. The bed was divided into 1000 adaptive layers with their own unique grain size distributions, thereby spatially resolving the bedding in detail. The model predicted the formation of stationary and downstream moving antidunes that occasionally would move upstream. The complex flow field, turbulence, free surface movement and sediment transport would then result in a bedding that included lenticular shapes. The numerical model explained the formation of this bedding with high spatial and temporal variation in velocity, turbulence, pressure, bed sediment size fraction together with water surface and bed movements.

Keywords: sedimentary structures, numerical modelling, sediment transport, Navier-Stokes equations, antidunes, lenticular structures.

1. INTRODUCTION

Sediment particles transported by rivers can form deposits that shape the landforms. Particles of varying sizes are deposited in a succession of high and low water discharges with different transport capacities. The result is the formation of layered sedimentary structures that can be seen in vertical cuts of the landscape (Collinson & Mountney, 2019). Several different sedimentary patterns exist, studied in detail in the science of sedimentology (Campbell, 1967).

An example is given in Fig. 1a, showing the Wingerbertswand near Mayen in Germany. This is a man-made excavated vertical wall in a quarry where the sediments were used for construction purposes. The figure shows near-horizontal lines of different greyscale and sediment size. How are such sedimentary structures formed and which physical processes are involved? The prevailing theory is that the sediments in the Wingerbertswand have been deposited by water in the upper flow regime, where the flow is critical or supercritical (Schmincke et al., 1973). This means that the Froude number (Eq. 1) is close to or above unity and antidunes/chute-and-pool systems can form.

$$Fr = \frac{U}{\sqrt{gy}} \tag{1}$$

U is the depth-averaged velocity, y is the water depth and g is the acceleration of gravity (9.8 m/s^2).

Looking closely at Fig. 1, the near-horizontal lines are not all completely straight. Several lens-like structures can be seen, two of which are indicated by yellow lines in the figure. Many sedimentologists have interpreted such structures to be formed by antidunes, chute-and-pools and cyclic steps bedforms, as the water surface waves move upstream (Cartigny et al., 2014). This interpretation, however, is not uncontroversial. Frechen (1971) believed the Wingerbertswand structures were formed by the wind. The current study shows in detail how wavy sedimentary structures and lenses can be formed by water in near critical flow, producing shapes similar to observations from the Wingerbertswand.

Figure 1. Photograph of the Wingerbertswand, showing lenticular structures (marked as yellow ovals).

Several research groups have studied geological formations deposited by water at high Froude numbers (Alexander & Fielding, 1997; Fielding, 2006, Xavier et al., 2022). Recent work includes Hovikoski et al. (2023), who described a number of different sedimentary structures formed by meltwater in subglacial channels under non-full pipe conditions, or by density currents. The sediments showed typical upper-flow-regime bedforms such as sinusoidal stratification, sigmoidal cross-stratification, scours with backsets or chaotic fill, interpreted as deposits of antidunes, humpback dunes, chutes-and-pools and cyclic steps. Lenticular beds of sandy gravel were locally present. The lenses were commonly 30–50 cm wide and ~10 cm thick. It is coincidental that this is the same size as observed in the result from the current study.

Bucher et al. (2024) observed lenticular structures from volcanic-sedimentary deposits. The particles were fragments from volcanic eruptions, which also melted ice, resulting in fluvial sediment transport. Lenticular bodies internally composed of steeply dipping backsets and concentric trough fills were interpreted as deposited by supercritical flows.

Scientific investigations of the formation process for sedimentary structures under near-critical flow conditions often use laboratory studies or numerical models. Examples of physical modelling of sediment deposits include Alexander et al. (2001); Leclair (2002); Baas et al. (2016); and Yokokawa et al. (2010). The studies confirm the formation of wavy sedimentary structures with lenses deposited in channels with near-critical flow. However, the physical models can only partly explain the process. Detailed measurements of grain size distribution, turbulence and water velocity patterns are difficult to obtain in the laboratory models with a moving bed and water surface (Alexander et al, 2001). An alternative to the laboratory experiment is to compute the formation of the sedimentary structures with a numerical model. This is done in the current study.

Recent use of numerical models in fluvial geomorphology includes Han et al. (2023), who computed geometric changes in the braided section of the Yarlung Tsangpo River in China. The main focus of the study was on lateral migration of the channels, which was modelled with a 2D depth-averaged program. Upper flow regime systems with riffle-pool formations have also been studied by Booker (2001). None of these models computed bedforms in detail or the sedimentary structures formed by the channels.

Movement of dunes in rivers and channels with sub-critical flow (Froude numbers well below unity) have been computed numerically by several researchers: Kopmann (2020); Giri & Shimitzu (2006); Ruehter et al. (2008); Nabi et al. (2013); Naqshband et al. (2015); Warmink et al. (2014). These studies focused on the determination of the height, length and migration speed of the bedforms. Other studies have used similar

technologies to compute sedimentary structures in alluvial channels with critical and supercritical flow. Olsen (2017a) computed the formation of downstream-moving antidunes. The resulting antidune height, length and celerity compared well with a physical model study. Vellinga et al. (2018) computed cyclic steps in a steep channel using the Flow-3D software. This commercial CFD program computed the complex water surface location using a volume-of-fluid method. One sediment size was used in the movable bed. The bed levels were recorded at different times, and by assembling these data, a combined image gave a visual view of the sedimentary structures. Slootman et al. (2021) used the same technique to compute cyclic steps in a channel where the slope changed from steep to mild. The sedimentary structure formed in the process was documented with the same method as Vellinga et al. (2018). Recently, Schwarzmeier et al. (2023) reproduced small-scale experiments with upstream-moving antidunes using particle-resolved simulations with homogeneous spherical particles. The same antidune results were found by Escauriaza & Williams (2024) using a simpler numerical model coupling the shallow-water and Exner equations in two dimensions.

The reason why sedimentary structures are seen in Fig. 1 is the formation of layers with different grain size distributions. The layers with coarse material are darker than the ones with finer particles. Detailed modelling of the process forming these structures should therefore preferably use multiple sediment sizes. This was done by Olsen (2022), computing sedimentary structures formed by downstream-migrating antidunes. The bed layer was resolved using up to 1000 vertical cells and five sediment sizes for each layer. The sedimentary structures given by different grain size distributions were therefore computed directly by the numerical model. The same technology is used in the current study.

Wavy sedimentary structures and cross-lamination have often been attributed to the existence of dunes in a fluvial setting (Leclair, 2002). As dunes move downstream at varying velocities, sand slides in front of the dune will form a bedding that dips in the downstream direction. The next question is then what causes an upstream-dipping bedding? A common assumption is that they are formed by antidunes, as these bedforms can move in the upstream direction. Olsen (2022) showed with a numerical model that upstream dipping bedding can be formed by downstream-migrating antidunes, where small bed waves form layers over the antidunes as they move downstream.

The current study uses the same numerical methods as Olsen (2022). A new upstream boundary condition has been introduced, producing a lower wave number for the antidunes. This has led to formation of lenticular sedimentary structures. Details of the formation process are given in the following, including complex velocity fields, turbulence, bed shear stress,

non-hydrostatic pressure, changes in the water surface elevation together with sediment sorting, deposition and erosion.

The main novelty of the current paper is that it uses an advanced numerical model to explain the hydrodynamics and mechanics behind the formation of lenticular sedimentary structures related to antidunes. Very few numerical simulations have captured the dynamics of antidunes, but even less have been performed considering different grain size classes predicting the formation of sedimentological structures.

2. METHODS

Numerical model

The numerical model was based on solving differential equations in two dimensions using a finite volume approach. The sediment transport was computed from a convection-diffusion equation for each of five different particle sizes: 0.5, 1, 1.5, 2 and 2.5 mm. The sediment pick-up rate was computed from the Engelund-Hansen (1967) formula. This procedure computed in principle the total load, but since the fall velocity of the particles was fairly large, the sediment would only have a significant concentration in the bed cell. The sediment transport mode was therefore bed load, similar to what was observed in the laboratory experiment of Núñez-González (2012) with downstream migrating antidunes.

The Navier-Stokes equations were solved to compute the water flow field, using the k-epsilon model (Launder & Spalding, 1974) to compute the turbulence and the bed shear stress. A structured non-orthogonal 2D width-averaged grid was used with 700x25 cells in the horizontal and vertical direction, respectively. An algorithm based on the water continuity in the top cells was used to compute the changes in the water surface elevation (Olsen, 2015). The changes in the bed level and water surface elevation were used to modify the computational adaptive grid over time. Further details are given by Olsen (2022). Note that the model has previously been verified against laboratory measurements computing antidune height, length and celerity of antidunes in a flume, together with the average water depth (Olsen, 2017a). The model has also been verified against measurements on other cases in the field of geomorphology, for example modelling a braided river (Olsen, 2021).

The sedimentary structures were computed using a high-resolution 2D grid of the bed sediments. The horizontal resolution was the same as the grid used to compute the water velocities. The 1000 bed cells were initially evenly distributed vertically on a 10 cm thick sediment layer. Each layer had an equal 20 % fraction, f, of the five sediment sizes. The composition and size of the bed layers changed as erosion and deposition

occurred over time. Erosion could cause the top bed cell to be reduced in size or cause it to disappear completely if a sufficient amount of erosion was predicted. Removal of one or more top layers over time meant that the total number of vertical bed layers could be reduced to under 1000.

Sediment deposition led to the formation of a new bed layer composed of the deposited material. Thus, the total number of layers could potentially exceed 1000, which was not allowed in the numerical model. Therefore, two of the original layers had to be merged. The two layers chosen were those with the smallest grain size difference, G_k, defined by the following formula:

$$G_k = \sum_{j=1}^{5} \left(f_{k,j} - f_{k-1,j} \right) \quad (2)$$

The index j denotes the number of the grain size, where 5 sizes were used in the current study. The new layer would have the same vertical magnitude as the two previous layers combined. The grain size distribution in the new layer would be a mixture of the two original layers.

Sedimentary structures would form from lines of equal grain size distribution, similar to what has been observed in nature (Fig. 1). Fig. 2 shows a detail of the resulting structure.

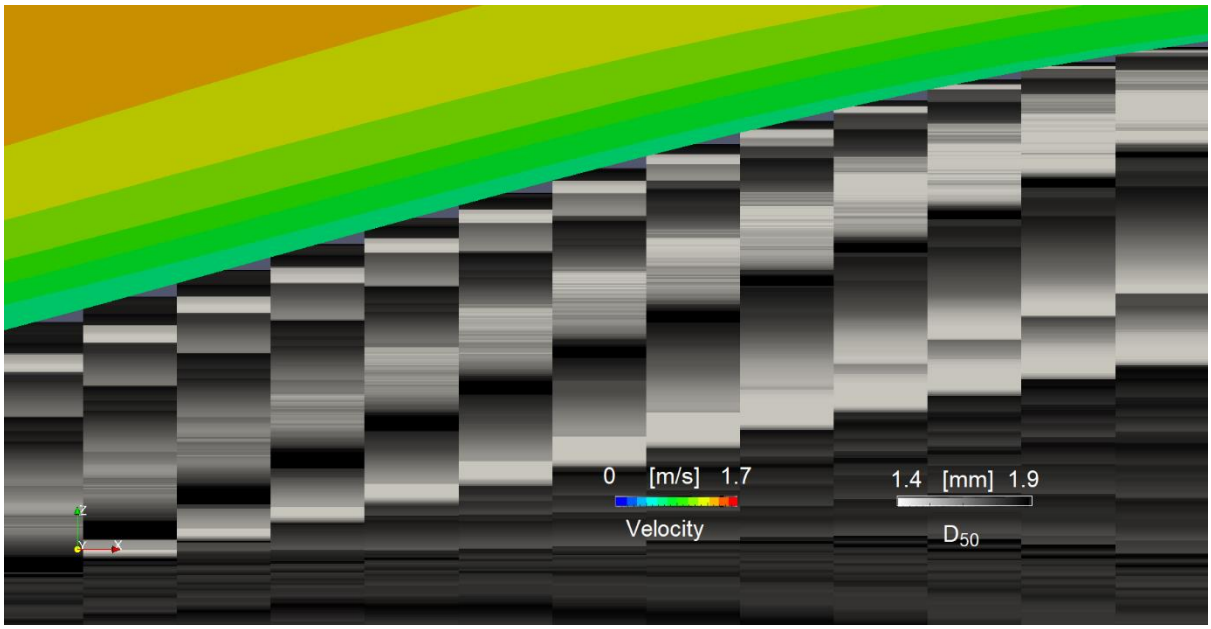

Figure 2. Detail of the bed grid. The colors show the water velocity above the bed. The different bed layers are shown with a greyscale, indicating the d_{50} of the particles. The horizontal size of the cells is 1 cm.

The numerical model was tested on a geometry similar to the laboratory study of Núñez-González & Martín-Vide (2010). The average water depth was 0.109 m and the water velocity was 0.97 m/s. This gave a Froude

number of 0.94, just below the critical value of 1. The flume was 0.75 meters wide and 28 meters long, but only the most upstream 7 meters were modelled numerically. This meant that boundary conditions were important. The same boundary conditions were used in the current study as Olsen (2022), except at the upstream boundary. In the current study the upstream values of turbulent kinetic energy *k* and turbulent dissipation rate *epsilon* were set to 0.2 m^2/s and 0.1 m^2/s^2, respectively. This was higher than in the previous study using 0.0025 m^2/s and 0.00039 m^2/s^2 for the same parameters. The actual turbulence values in the flume study were not known, so both sets of the values were guessed. A higher *k* value meant that the bed shear stress at the upstream boundary was larger than in the previous study, giving higher sediment transport capacity. The inspiration for changing the inflow turbulence was a replication of the upstream boundary condition of the laboratory model. The water inlet in the laboratory flume included a layer of porous bricks. The water was partly flowing through the bricks and partly over the bricks, giving an increase in turbulence. An upstream wave formed downstream of the bricks, giving a water surface slope that was positive in the downstream direction. A sketch is given in Fig. 3. The boundary condition in the current study tried to replicate the shape of this slope. The most upstream water level, *z*, was given a low value and a smoothing algorithm was used in the 30 following cross-sections according to the following formula:

$$z_{i,new} = 0.25\, z_{i-1} + 0.5\, z_i + 0.25\, z_{i+1} \qquad (3)$$

The grid line numbering is indexed with I in the main flow direction. The upstream water surface was thereby lower than in the previous study (Olsen, 2022). The effect is discussed further in Chapter 4.

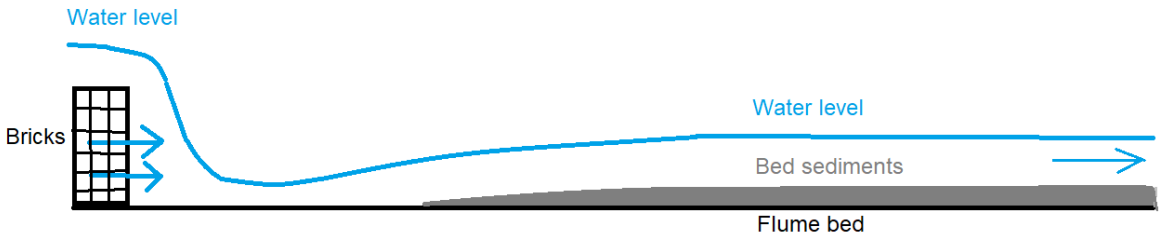

Figure 3. Sketch with longitudinal profile of the upstream end of the flume. The arrows show the velocity direction.

The production of sedimentary structures required hydraulic conditions where deposition of particles occurred. This was done by giving an inflow sediment concentration that was higher than the transport capacity of the

flume. Giving a too high concentration would cause a large increase in the slope of the bed. While a too low concentration would not produce a sediment deposition. A trial-and-error method was used to find the inflow concentration of 0.07 % by volume for each particle size.

Description of bed configurations

The bedforms developed in the simulations were identified individually using an algorithm that defined a disturbance in the bed profile with a maximum between two minima. The crests of the bedforms were defined where the bed level in one cell was larger than the eight upstream and downstream cells. The bedform height was calculated as the difference between the average elevation of the minima and the elevation of the maximum, while the length was determined by the horizontal distance between the two maxima. This method was used to calculate the average heights and wavelengths of all length scales of bedforms along the profile at each time step.

To determine the characteristic heights and wavelengths of dominant mesoscale bedforms at a given time-step and profile reach, two methods were used. First, dominant wavelengths were obtained through spectral analysis using a fast Fourier transform. Then the characteristic heights were calculated as a function of the standard deviation (σ) of the elevations in the longitudinal profile. This approach assumes that the profile of the dominant bedforms approximates a sinusoidal shape, as is commonly seen in antidunes. Following Willis & Kennedy (1978), the height of the bedforms was then calculated using the formula

$$h_b = 2 \cdot \sqrt{2} \cdot \sigma \qquad (4)$$

The direction of movement of the bedforms in the simulations was compared with the theories of Kennedy (1963) and Núñez-González & Martín-Vide (2011). According to Kennedy's theory, the maximum Froude number for antidunes to move against the current is given by:

$$F = \frac{1}{\sqrt{y \cdot k}} \qquad (5)$$

An alternative formula was given by Núñez-González & Martín-Vide (2011):

$$F = \frac{1}{y \cdot k} \qquad (6)$$

where y is the water depth and k is the wave number, defined as $k=2\pi/L$, with L being the wavelength of the bedform. The two versions of the

Froude number are used later in the analysis of the migration direction of the antidunes.

3. RESULTS

Bed and water surface configurations

The results of the entire computation (2714 time steps, 6785 s, approximately 113 min) are shown in Fig. 4, with longitudinal profiles of the flume at different times (Fig. 4a; an animation of the entire simulation, including these profiles, is provided as supplementary material) and space-time plots of the water surface and sediment bed (Fig. 4b-e). Fluctuations of bed and water elevations in the space-time plots are shown relative to the instantaneous streamwise average, which was determined by fitting linear least-square trend lines to the instantaneous profiles. From these lines, a time-averaged bed sedimentation rate of 0.04 mm/s was computed and bed slopes ranging from 0.013 to 0.026 were obtained. Average water depth was 0.079 m. The bed was initially flat, as shown at 25 seconds (Fig. 4a). Bedforms then began to emerge and develop over time. The initial bed features were small, but they quickly grew larger over time, both in height and in length. The water surface mirrored the bed configuration (Figs. 4a-c), showing that bed and water profiles were in phase, which is a defining characteristic of antidunes.

Figures 4d and 4e provide a closer view of the timescales associated with the free water surface and bed configurations. On the free surface, small, roughly triangular disturbances appear on the crests of surface waves. These triangular disturbances correspond to upstream moving surface waves, as shown in the profiles of Fig. 4a at times 2175 and 2450 s, over the sixth bedform from upstream. A closer examination of Fig. 4b, which covers the entire simulated time domain, and a comparison with zoomed-in views, such as Fig. 4c, reveal that these upstream moving surface waves form a series of disturbances that seem to migrate upstream. The imprint of one of these groups of disturbances is marked by a dashed arrow in both Fig. 4b and Fig. 4c, as the same series of disturbances also leaves a mark on the spatio-temporal graph of the bed. Regarding the time zooms of the bed profile (Fig. 4e), they show that small-scale bedforms develop on top of the primary mesoscale bedforms, mainly from the middle of the channel to its downstream end. These secondary bedforms seem to dominate in the last two meters of the bed profile.

A close observation of the profiles in Fig. 4 shows that the amplitude of the dominant bedforms increased with downstream distance, reaching stable conditions approximately between x=3 m and x=4 m. Thus, the channel can be divided at x=3.5 m into two reaches with bedforms of similar characteristics. The coexistence of bedforms with different scales and characteristics along the channel is evident in Fig. 5, where the

temporal variation of the mean instantaneous values of height and wavelength for the individual bedforms is shown. In the same figure, the wavelengths and amplitudes of the dominant bedforms in the two reaches separated by x=3.5 are plotted (the immediate reaches after the entrance and before the exit of the channel were not considered to avoid the influence of boundary conditions). It is clear that the dominant bedforms are subsets of the bulk of bed features, with those in the downstream section having higher amplitude but shorter wavelength than those in the upstream section. Additionally, Fig. 5 shows that heights and wavelengths stabilize after approximately 4000 s (66 min).

An evident difference between the primary and smaller-scale secondary bedforms is that the latter always migrate downstream (in Fig. 4e, the spatio-temporal fringes of crests and troughs describe a positive slope), while the primary bedforms either remain stationary or migrate both downstream and upstream. They move downstream from the beginning of the simulation until 2000 seconds, and then, after 2000 s, some of them —mainly those at x<3.5 m —move upstream for short periods (the spatio-temporal fringes of crests and troughs describe a negative slope, as seen in Fig. 4c). At around t=3000 s, the primary bedforms stabilize and remain nearly stationary (the spatio-temporal fringes of crests and troughs become approximately vertical). The lenticular structures we focus on in this work developed between x=2.5 and x=3.5 m, between t=2000 and 3000 s, as will be seen below. This period and zone correspond to where the primary bedforms are most erratic in their direction of motion and unstable in their geometry. It will be shown later that this instability is crucial for the formation of the lenses.

Figure 6 shows the dominant bedforms at each time step as a function of the wave and Froude numbers, distinguishing between the profiles upstream and downstream of x=3.5 m. Bedforms for t>4000 s are also given in the figure, which is the time from which the geometry of the bedforms becomes approximately stable. Theoretical curves that delimit the direction of movement of the antidunes are also shown. The two theoretical boundaries for upstream-migrating antidunes indicate a boundary strip separating the bedforms upstream and downstream of the channel's center. Most of the antidunes at x <3.5 m are close to the lower theoretical curve, while the bedforms at x>3.5 m mostly appear to be in the region of downstream-migrating antidunes. Thus, the migration of the bedforms in the simulations aligns well with theory: antidunes in the upper channel reach were mostly stationary but migrated upstream at certain points, which agrees with their proximity to the boundary for stationarity. Antidunes in the lower channel reach were stationary with a slight trend to move downstream.

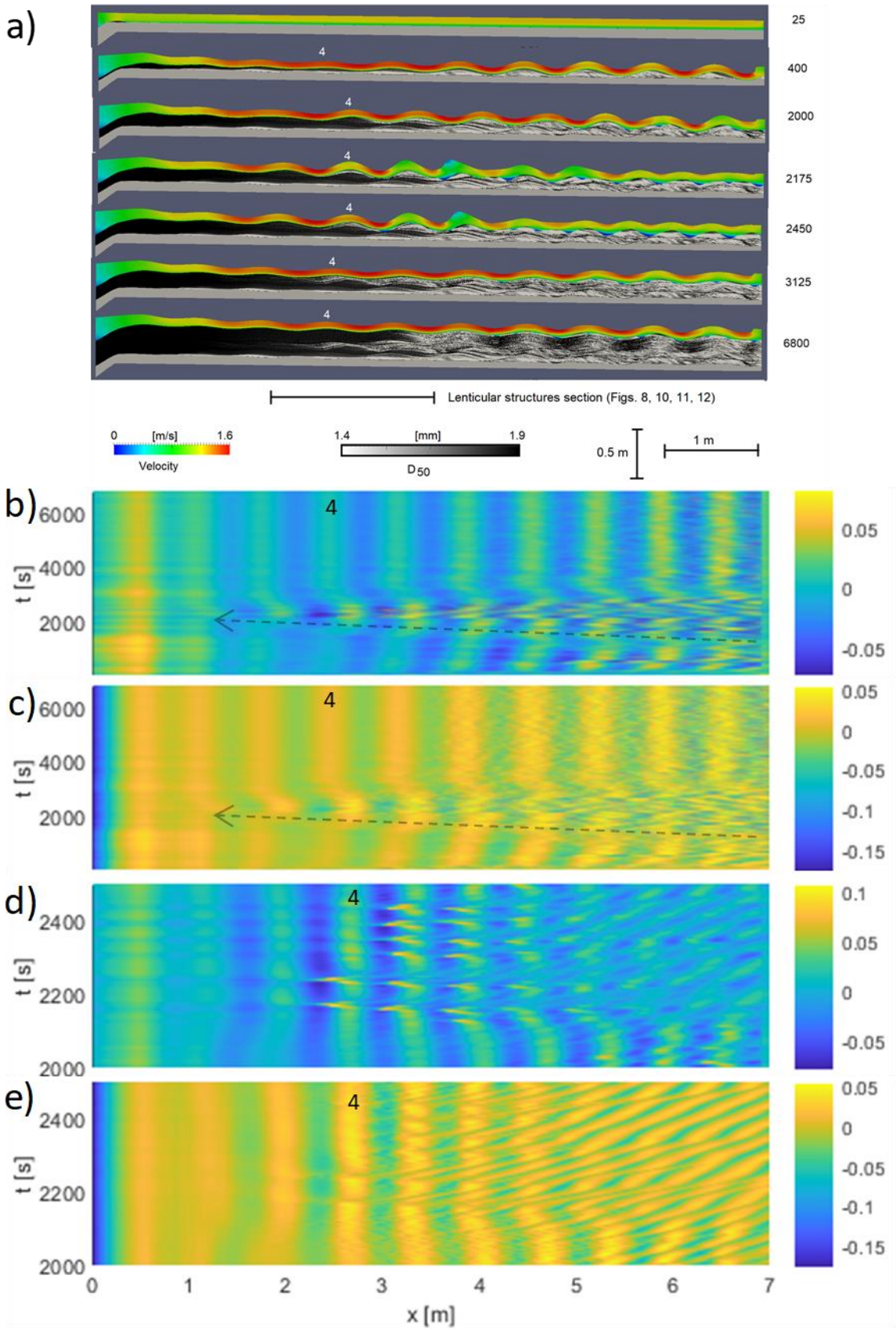

Figure 4. Longitudinal profiles of the computational domain at different time steps (seconds) (a), and space-time plots of the water (b, d) and bed (c, e) surfaces. The water flow direction is from left to right. The number 4 is the fourth antidune from the upstream side. A video from

Fig. 4a is given in the supporting material. Plots (b) and (c) were smoothed with a moving average over 5 time intervals (12.5 s).

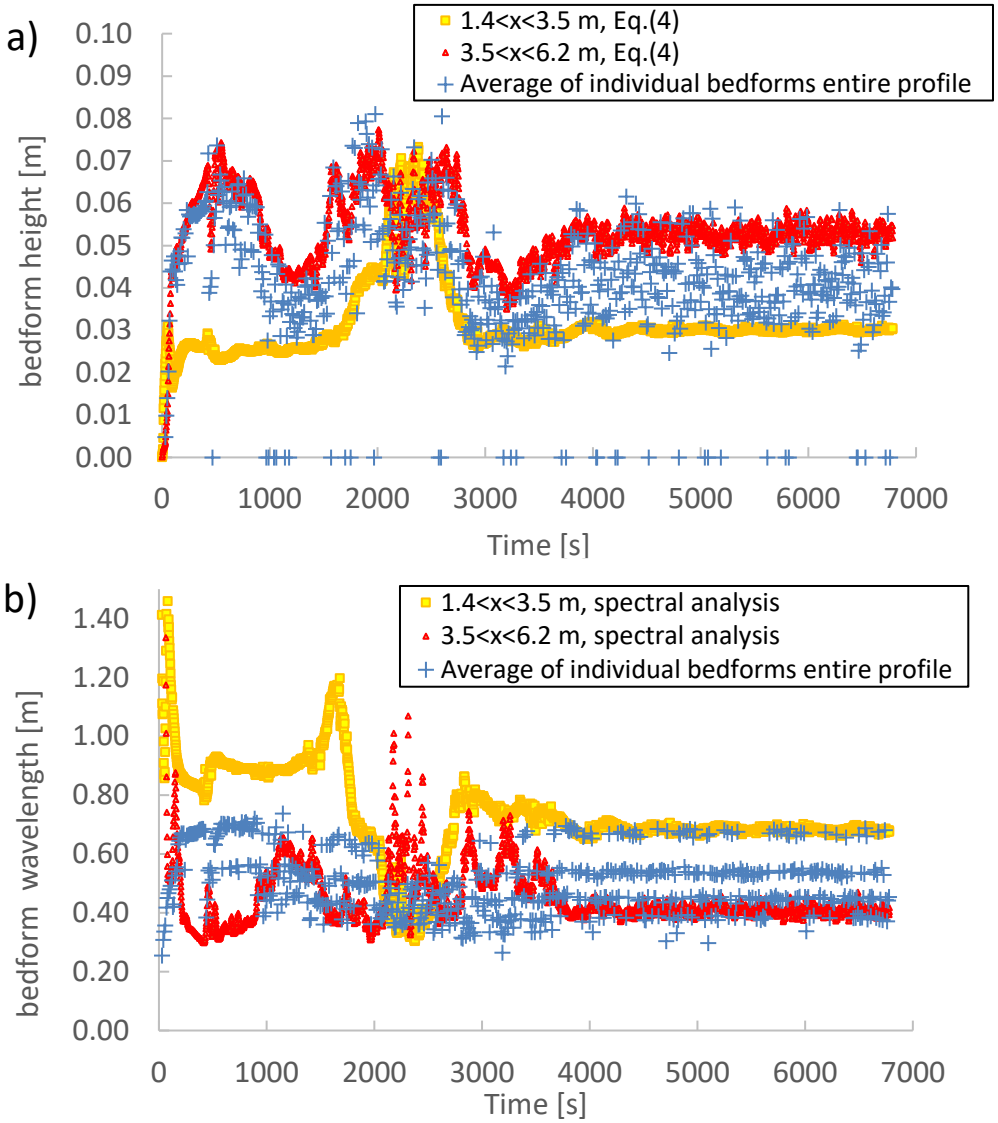

Figure 5. Time evolution of bedform height (a) and wavelength (b), calculated using different methods and for different bed reaches. Spectral analysis and the bed standard deviation were used to obtain dominant bedforms, while individual bedforms were computed with an algorithm to distinguish maxima and minima heights (see chapter 2).

Flow and sedimentary structures

The colors in Fig. 4a show the water velocities, indicating higher values at the water surface due to the friction at the bed. It is also interesting to see that the surface velocity is higher in the troughs than over the crests. This is due to energy considerations. The potential water energy of the

water at the top of the crest is higher than the similar value in the trough. The potential energy over the crest is transformed to kinetic energy, giving higher velocity in the through. The difference in the velocity between the crest and the through is therefore a function of the antidune height. This can be seen in Fig. 4a, for example in the velocities at 400 seconds. The antidunes are higher and have lower crest velocities in the downstream end than further upstream.

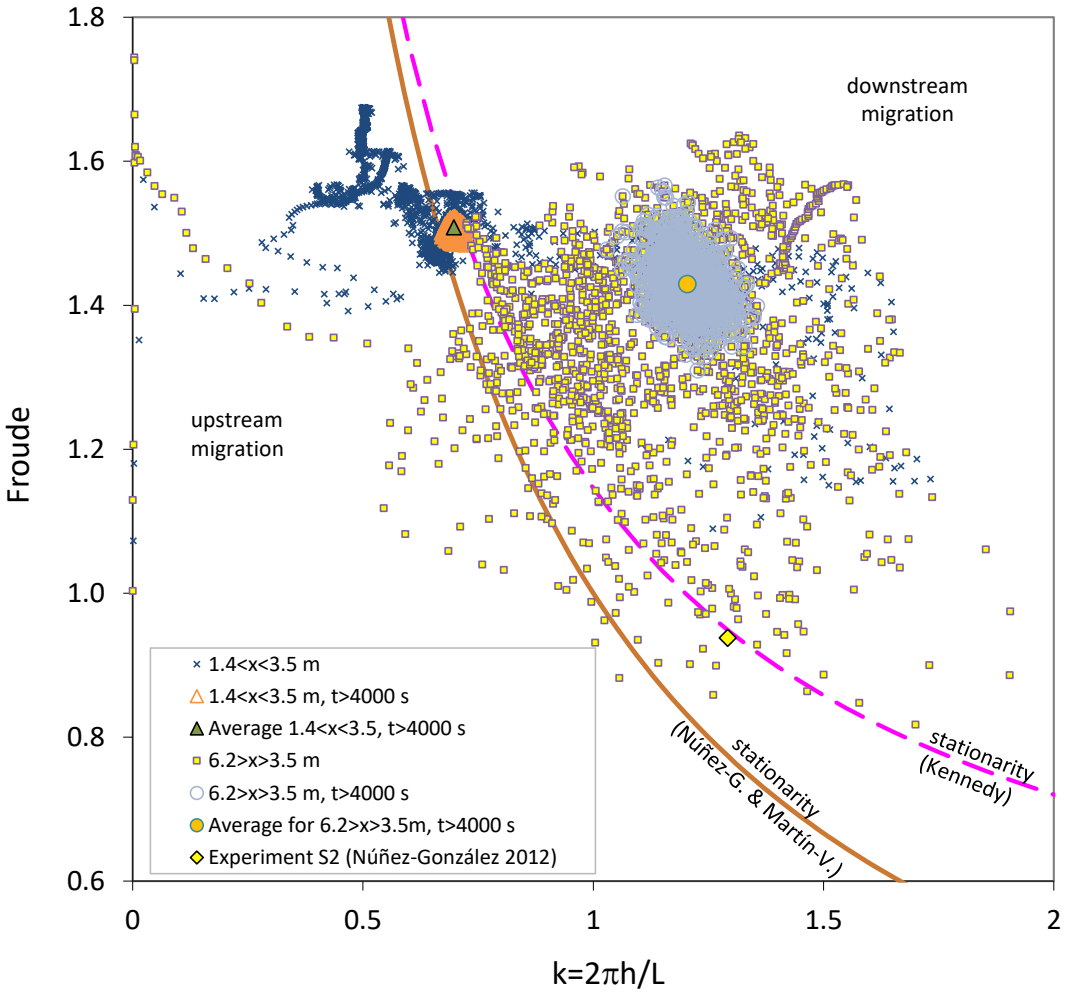

Figure 6. Plot of the simulated dominant bedforms at each time-step on the theoretical stability diagram that delimits upstream- and downstream-moving antidunes.

A longitudinal profile of the turbulent kinetic energy, *k*, and its variation over time is given in Fig. 7. The figure shows the relatively high value of *k* at the inflow, which caused high shear stress at the bed and reduced deposition at the upstream end. The earlier described algorithms (Eq. 3) for lowering the upstream water level led to a positive water surface slope. This meant that the total bed slope was lower than in the previous computation by Olsen (2022).

Figs. 4a and 7 show the d_{50} of the bed grain size distribution in greyscales. The sedimentary structures can thereby be seen, similar to observations in the field given for example in Fig. 1. Most of the structures are formed by smaller low-relief waves moving on top of the antidune bed (secondary bedforms identified in Fig. 4e). Details on these processes are described by Bridge & Best (1997), Alexander et al. (2001), Lunt & Bridge (2007) and Olsen (2022).

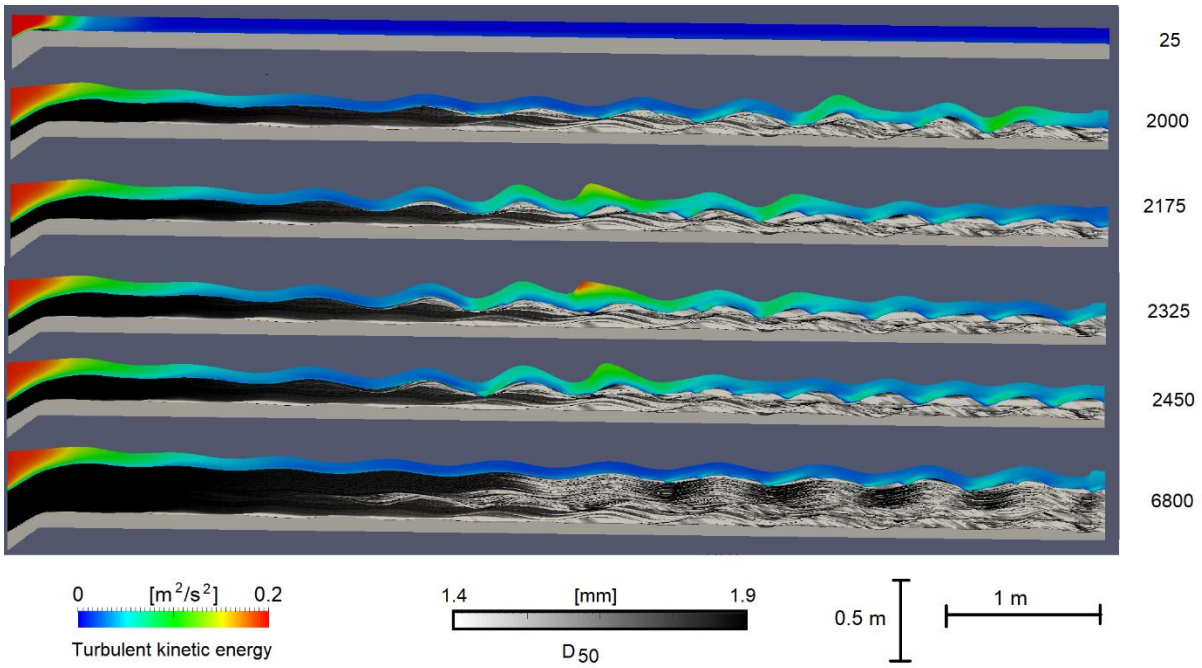

Figure 7. Longitudinal profile of the computational domain at different time steps (seconds), where the colors show the turbulent kinetic energy, k. The water flow direction is from left to right.

Figs. 4a and 7 show the whole length of the flume, making it difficult to see the formation of the lens in detail due to the scale. More detailed views of the profiles close to the lens are therefore given in Figs. 8-11.

Fig. 8 shows a longitudinal profile at the location where the two lenticular structures formed (2<x<3.5 m). For comparison, time series of wavelength and height of the dominant bedforms in the upper reach are plotted in Fig. 9. Fig. 8 shows that the antidunes were slowly moving downstream up to 2000 seconds. The initial antidunes at 25 seconds were small, but they grew larger over time, both in height and length, as seen in Fig. 9a. At 2000 seconds the antidunes appear fully developed, with wavelengths and heights remaining relatively constant for several minutes, as shown by the plots in Fig. 9a with short plateaus. Shortly thereafter, the antidunes rapidly increased in height and decreased in wavelength, but by 3000 seconds, the inverse occurred: they have decreased in vertical size and increased in length. The formation of the lenticular structures took place between 2000 and 3000 seconds. After

3000 seconds, when the bedforms stabilized, only wavy laminae of uniform thickness formed in the stratigraphy of that zone.

More details about the formation of the lenticular structure are provided in Figs. 9b and 10, showing the evolution of the bed and dominant bedform characteristics between 2000 and 3000 seconds. Between 2075 and 2150 seconds, Fig. 9b shows that the antidunes grew vertically and decreased in wavelength, but this trend was reversed several times thereafter, evidencing an oscillation in height and wavelength. Note that antidune height and wavelength show a negative correlation, so that as the bedforms grew, their wavelength decreased, and vice versa. The profile in Fig. 10 shows that between 2000 and 2220 seconds, there was an increase in the difference between the water flow velocity at the through and the crest. This corresponds with the preservation of total energy as the sum of velocity (kinetic) and potential (vertical level) energy. Also note that the antidunes moved downstream, according to the hydraulic conditions given for this case.

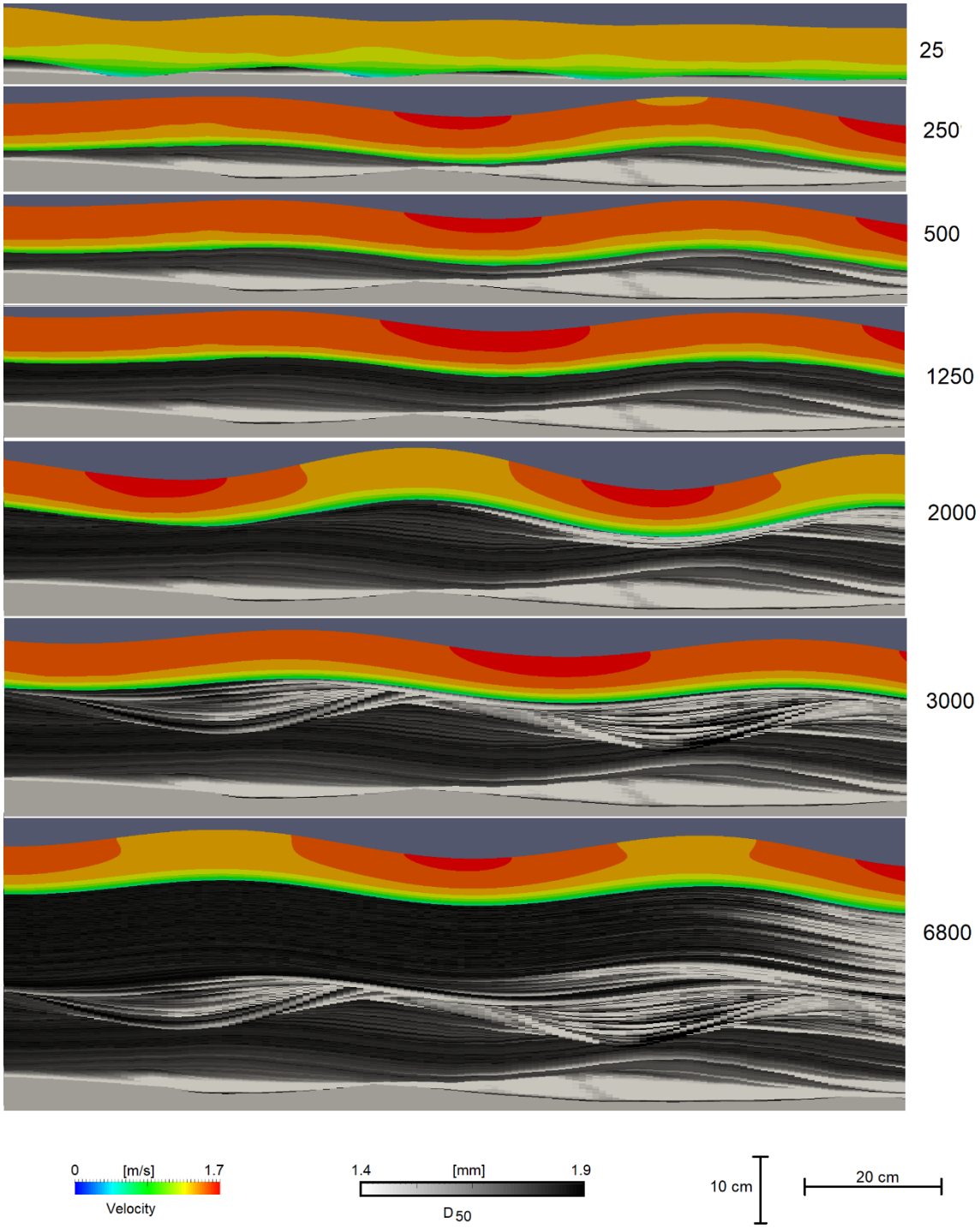

Figure 8. Longitudinal profile of the flume close to the lenticular structure at different times, where the colors show the water velocities. The flow direction is from left to right. A video of this figure is given in the supporting material.

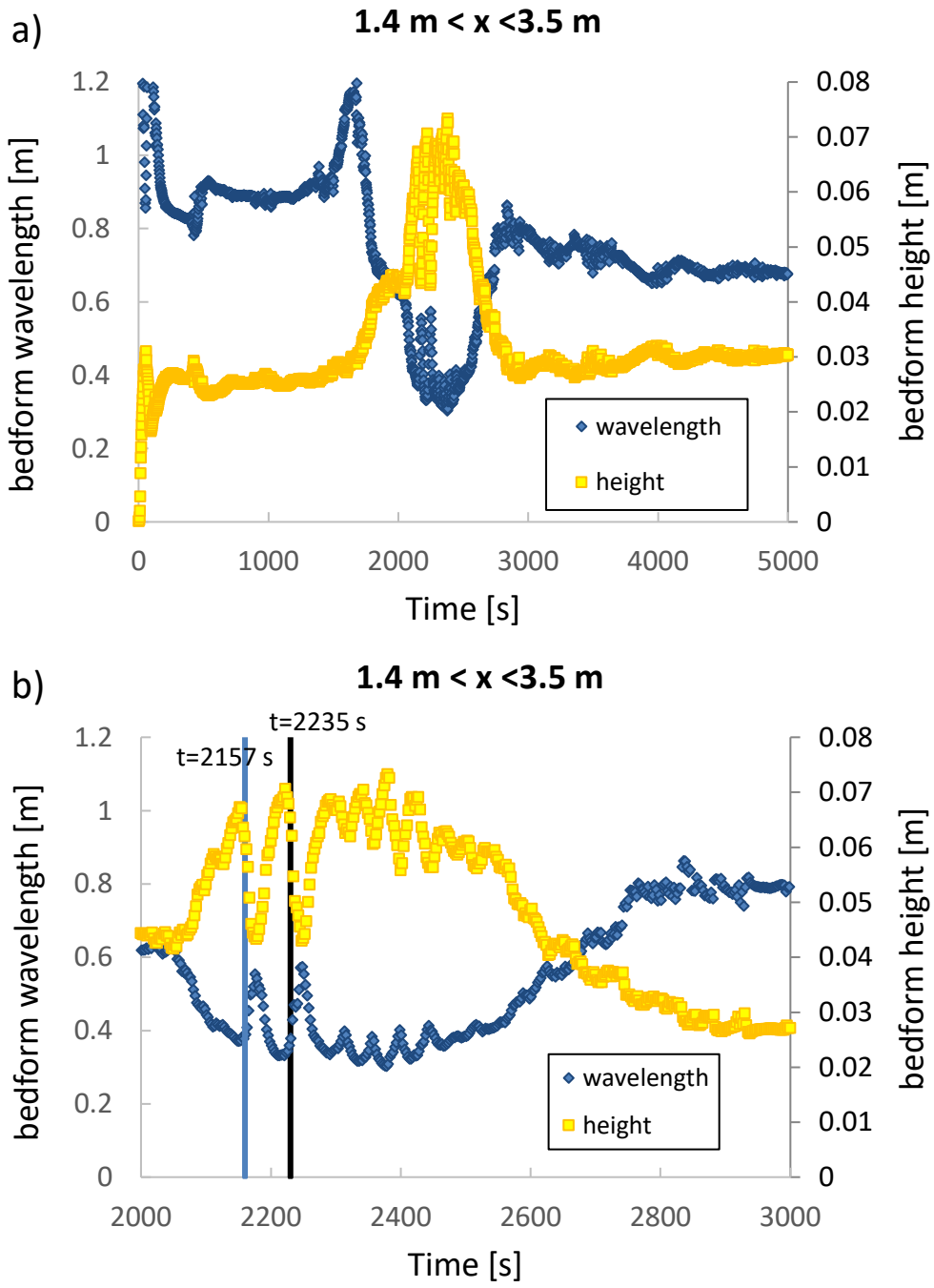

Figure 9. Time evolution of height and wavelength of the dominant bedforms in the upper reach of the channel. Parameters obtained through spectral analysis and the bed standard deviation (Eq. 4).

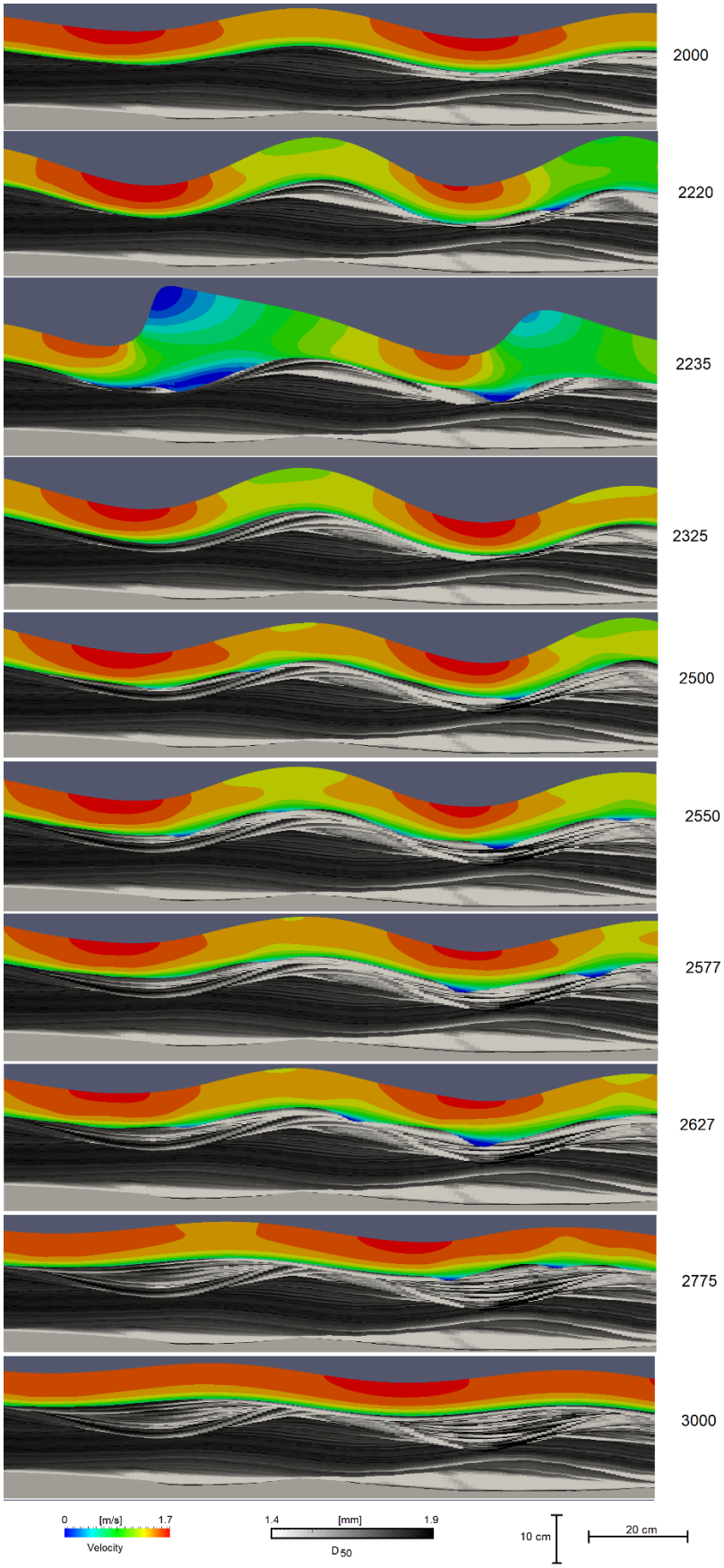

519
520 *Figure 10. Longitudinal profile of the flume close to the lenticular*
521 *structure at its formation. The flow direction is from left to right.*

The initiation of the lenticular structure starts with an upstream moving surface wave. This is seen in Fig. 10 at 2235 seconds. The wave in the middle of the figure has moved slightly upstream. The velocity at the crest given with blue color has decreased considerably. The surface wave moved much faster than the wave bed as the sediment transport velocity was slower than the water velocity. However, due to the low water velocity at the upstream side of the antidune bed, the sediment deposited there. The bed wave therefore moved slightly upstream. During this process, the trough upstream of the antidune was filled. This is shown in Fig. 10 from 2325 to 2600 seconds.

The same wave at 2235 s in Fig. 10 can also be identified in Fig.4d. It is part of a series of successive upstream moving surface waves over time and space. Of these waves, the upstream moving wave shown in Fig. 10 occurred at 2230 s at x=2.5 m, and a second wave in the same position occurred before at 2160 s. The time steps when these two upstream moving waves occur are indicated in Fig. 9b by vertical lines. It is observed that the two waves coincide with maximum and minimum heights and lengths of the bedforms, respectively. As an antidune grew, the amplitude of the wave above it also increased. When the surface wave reached a sufficiently large amplitude, it moved in the upstream direction, destabilizing the antidune. The sediment deposited in the upstream trough, due to the reduced flow velocity, might have caused a sediment deficit over the antidune, which in turn may have caused it to lose height and increase in length, as shown in Fig. 9b.

Upstream moving antidunes are often a non-stable phenomenon that only occurs over a short time period (Kennedy, 1963; Collinson and Mountney, 2019). Fig. 10 at 2325 seconds shows a stable situation where the water and bed level were in the same phase. The continuous feed of upstream sediments caused a layered sediment deposit in the through. Fig. 10 at time 2500 s shows a smaller bed wave moving on top of the antidune upstream of the crest. This wave deposits a layer of coarse and fine material. Two bed waves are seen at 2550 seconds after the bed has gradually increased in elevation. The bed waves have formed a layered structure, with lines roughly parallel to the bed surface. This process took place until 2600 seconds. During this time, the antidune was stationary and the growth was almost uniform over the length. However, the height of the antidune decreased, as can be seen comparing the times 2325 through 2600 in Fig. 9b and 10. The sediments were deposited in greater magnitude in the throughs than at the crests. This formed the lower part of the lenticular structure.

The upper part of the lenticular structure was formed between 2600 and 2627 seconds after the start of the computation, as seen in Fig. 10. The wave over the structure then shifted upstream. A new stable antidune

formed afterwards, which moved upstream too, as seen in Fig. 10 between 2627 and 3000 seconds. Therefore, the upstream movement of the antidune contributes to the preservation of the lenticular structure. By moving upstream, the antidune covers the lenses and prevents them from being eroded by the bedform trough.

The structure in the lenticular body was formed by smaller waves on top of the main antidune bed. This can be seen on the upstream side of the left antidune at 2500 seconds in Fig. 10. Two of these wavelets are also seen on both sides of the crest at 2550 seconds. At 2600 seconds, there is a small secondary wave on top of the antidune. These waves have earlier been described in physical model studies (Alexander et al, 2001) and numerical models (Olsen, 2022). The secondary bed waves moved downstream, sometimes eroding the existing bed structure. The wave deposited two layers: one coarse and one fine. The lines in the lenticular structure of Fig. 10 are made up of such layers.

The formation of the small secondary bed waves can also be seen in Fig. 11, where the colors show the turbulent kinetic energy. The value of this parameter close to the bed is proportional to the bed shear stress (Rodi, 1980). Fig. 11 shows that the bed shear stress is high on top of the bed waves, and low in the front. The fine sediment will deposit in the front and then the coarse sediment will move over the fines. This creates two layers from one bed wave. Fig. 11 shows two bed waves at the upstream side of the central antidune. At 2750 seconds, there are five bed waves. These larger bed waves can produce the thicker layers in the sedimentary structure. At 3000 seconds, the antidunes have stabilized and the bed waves have become so small that they cannot be seen in the bed shear stress at Fig. 11. Looking at the end result at 6800 seconds in Fig. 8, the laminae above the lenticular structure are so small that they are hardly seen. Between 3000 and 6800 seconds, the antidunes were stable and a wavy deposition pattern formed.

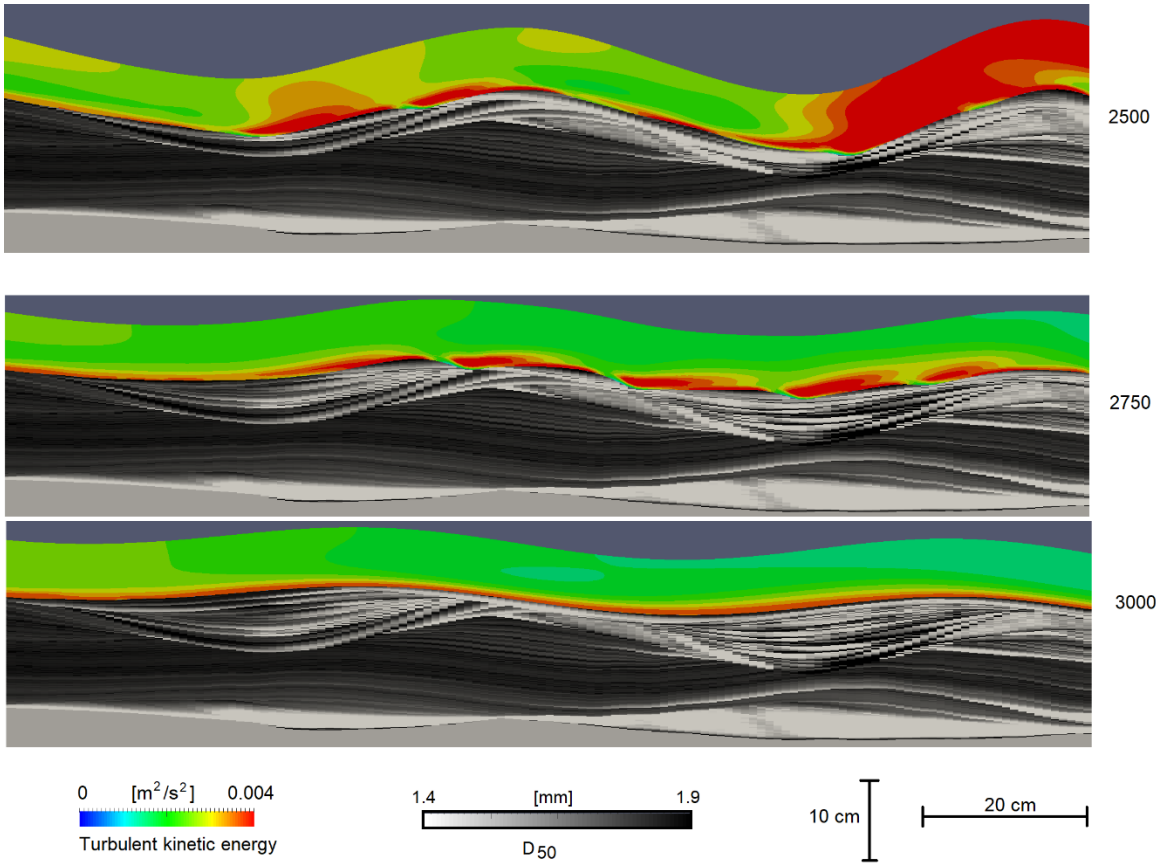

Figure 11. Longitudinal profile of the flume close to the lenticular structure at different times, where the colors show the turbulent kinetic energy. The flow direction is from left to right.

An interesting question is why the upstream-moving wave forms, as seen in Fig. 10 at 2235 seconds? Movement of a wave in a river can be predicted by looking at a control volume around a section of a channel (Olsen, 2017b). The forces on the volume are the hydrostatic pressure and the momentum from the water velocity on upstream and downstream side. Fig. 12 shows the computed pressure during the formation of the lenticular structure. The pressure is strongly non-hydrostatic, as can be seen by following the lines distinguishing the different colors. A hydrostatic pressure would mean that these lines would be parallel to the water surface. The numerical model also solves the Navier-Stokes equations in the vertical direction, enabling the computation of non-hydrostatic pressure.

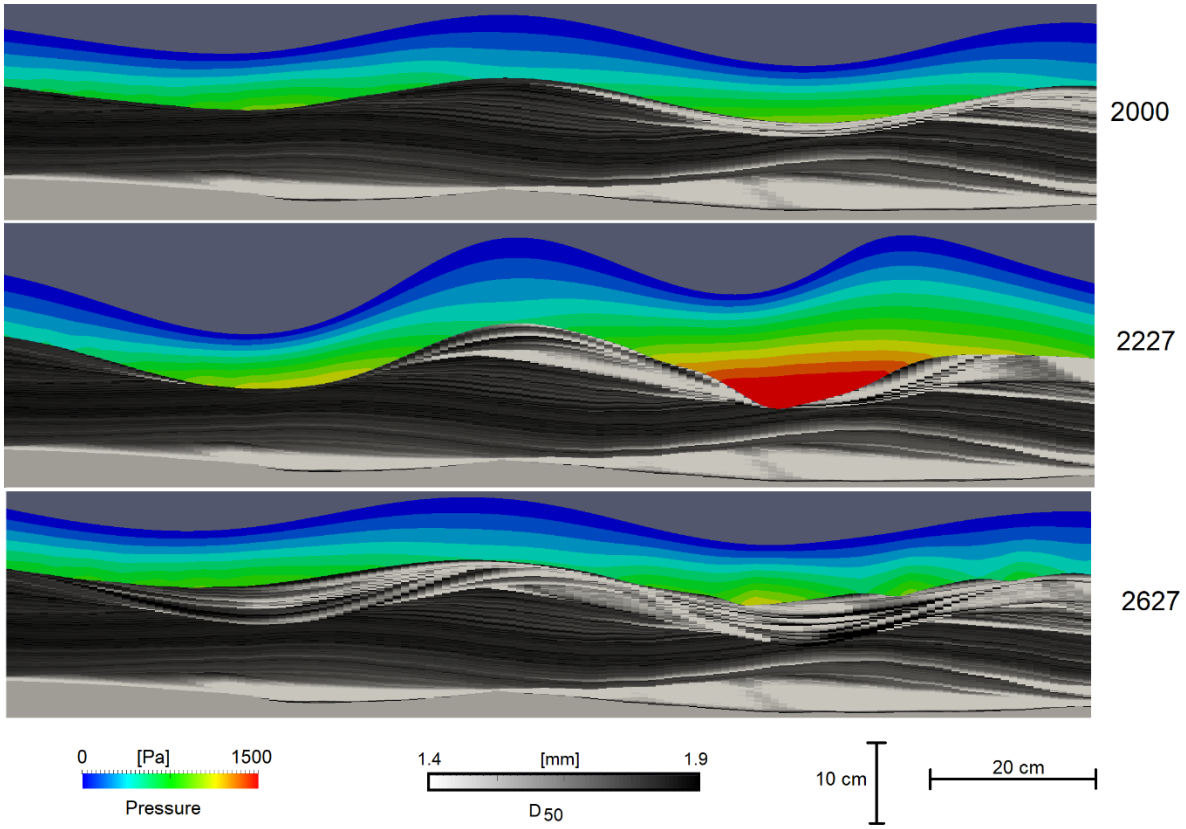

Figure 12. Longitudinal profile of the flume close to the lenticular structure at different times, where the colors show the pressure. The flow direction is from left to right.

Before (2000 seconds) and after (2627 seconds) the upstream-moving wave formed, the pressure was similar on both sides of the central antidune. The antidunes were stable and the water level was in phase with the bed. The image at 2227 seconds shows the longitudinal profile just before the upstream moving wave formed. There is an exceptionally high pressure on the downstream side of the antidune, pushing the water and water surface upstream. The increased pressure arises from the water velocity gradients at the location. In the SIMPLE method (Patankar, 1980), the numerical model transforms the water continuity defect (excess water) from the previous time step to a higher pressure in the through. The corrected velocity field thereby satisfies water continuity after the pressure has been increased. The numerical model replicates the physical processes in the flume, predicting the upstream movement of the surface wave and the antidune.

4. DISCUSSION

The current study presents a numerical model that predicts the formation of lenticular sedimentary structures. The model was previously validated against laboratory data (Núñez-González, 2012) for average antidune height, length and celerity. There is, however, no direct comparison between the geometry of the computed sedimentary structures and

similar results from the laboratory study. The results of the numerical model must therefore be evaluated by observations from scientific articles describing other laboratory studies of sediment deposits under critical flow conditions together with field observations.

A landmark laboratory study of sedimentary structure formation with high Froude numbers was carried out by Alexander et al. (2001). In connection with antidunes they observed lenticular laminasets – "lenses (laminasets) with erosional, trough-shaped bases that contain sets of laminae". Campbell (1967) define a laminaset as "a conformable succession of genetically related laminae that are bounded by laminaset surfaces". Alexander et al. (2001) observed from the laboratory studies that the laminae within the sets were up to a few millimetres thick, distinguished by slight variations in the particle grain size. The lenticular laminasets had concave-upward erosional bases. "Laminae that fill the troughs symmetrically are associated with surface-wave breaking and filling of antidune troughs". The description of Alexander et al. (2001) fits very well with the results of the current study. Furthermore, Alexander et al. (2001) recommends as tools for paleohydraulic reconstructions that the length and maximum thickness of the lenticular laminasets are approximately half of the length and height of formative antidunes. Looking at the size of the computed lenticular sedimentary structures in Figs. 8,10-12, they have a reasonable fit with the guidelines of Alexander et al. (2001).

A recent study of Xavier et al. (2023) describes sedimentary structures observed in an arid to semiarid ephemeral fluvial system in the southern Brazil. The different types of deposition patterns are classified in three facies with different parameters. One of the parameters is the observed lens size. Only the facies formed by unstable antidunes are associated with this parameter. The results correspond with the current study, where lenticular sedimentary structures are produced by an upstream-migrating antidune. Xavier et al. (2023) also presents a sketch (Fig. 16) showing longitudinal profiles of the channel during the formation of the lenticular structure, similar to what is shown in Figs. 8,10-12 of the current article. Although not founded directly on numerical or laboratory data, it shows that lenticular structures form over a bed with antidunes where the water wave move upstream and sediments fill the throughs. This is conceptually similar to the results from the current study.

Cartigny et al. (2014) observed formation of lenticular sedimentary structures without any lamination, which is not the same as the results of the current study. However, the formation process was different. Cartigny et al. (2014) described the lenses as formed by suspended particles, as their flume experiment used finer particles. The current study, modelling mainly bedload, therefore only described one possible formation process

for the lenticular sedimentary structures. Other hydraulic conditions may also produce these geological features.

The current study is an extension of the earlier work of Olsen (2022), who used the same numerical model as used in the current study to predict fractional sediment deposition under antidunes. Formation of sinusoidal sedimentary structures was produced, together with downstream and upstream dipping. The novelty of the current study is in the prediction of lenticular formations. These emerged due to the new upstream boundary condition with lower water levels and higher bed shear stress. The movement of the wave comes from the sum of forces in a control volume around the antidune. A lower upstream water level means a lower pressure force on the upstream side. This is why the upstream wave was stronger in the current computation compared with Olsen (2022), who used a higher upstream water level. However, is this possible in nature?

A natural river will often have much more complex geometry than a straight laboratory flume. There can be contractions in the river, forming small hydraulic jumps. There can be discontinuities in the bed slope. Also, there may be large boulders affecting the vertical and horizontal flow direction and water surface shape. It is therefore not unlikely that such positive water surface slopes may occur in nature.

One of the goals of the current study was to provide information about the processes creating lenticular sedimentary structures. The numerical model shows that the formation and preservation of these geological features is an indirect effect of the development of upstream-migrating surface waves. As demonstrated before, these surface waves result from a strong pressure gradient between the upstream and downstream flanks of the antidune. The formation of these pressure gradients and subsequent countercurrent surface wave migration coincide with the reach of the maximum height of the bedforms, as seen by comparing Figs. 9, 10 and 12 between 2227 and 2235 s. Therefore, considering both processes, we interpret that the pressure gradient and the upstream motion of the surface wave are related to the growth in amplitude of the surface wave in response to the growth of the antidune beneath it; when the wave reaches an unstable height, it collapses with a countercurrent motion. This collapse would be related to the upstream breaking of surface waves over antidunes, observed by other authors (Kennedy, 1963, Alexander et al, 2001). The numerical model applied here does not consider the intrusion of air into the flow, so it cannot simulate the wave breaking process. However, the model is able to reproduce the upstream motion of a surface wave, so it produces a similar effect on the antidune morphology that wave breaking would produce.

But why did the antidune move upstream for a short period? The decrease in flow velocity under the upstream moving surface wave reduced the transport capacity of the flow. As a result, sediment was deposited in the antidune trough and, the deficit of material on the crest caused the height of the antidune to decrease. This change in geometry resulted in an increase of the antidune wavelength, which decreased the wavenumber ($k=2\pi/L$) and therefore caused the antidune to move, from the downstream migration region to the upstream migration region in the diagram of Fig. 6.

The filling of the trough and decrease in height of the antidune related to the surface wave, also resulted in an increase in the radius of curvature of the bedform. Núñez-González et al. (2020) showed, with a specific energy diagram for antidunes, that as the radius of curvature of an antidune increases, the water depth over the crest tends to be larger than over the trough, so that the flow decelerates from trough to crest, producing sedimentation on the upstream flank of the antidune and causing it to migrate upstream. This upstream displacement of the antidune allows the preservation of the lenses.

The effect of the changing wavelength on the antidune movement is best recognized through the antidune mobility number, *Fa*, defined by Núñez-González & Martín-Vide (2011) to distinguish antidune movement regimes: antidunes migrate upstream if $Fa < 1$, downstream if $Fa > 1$, and remain stationary if $Fa = 1$. Núñez-González & Martín-Vide's used the criterion, $Fa = F \cdot k$, while Kennedy's (1963) criterion as a function of *Fa* yields, $Fa = F \cdot k^{0.5}$.

Figure 13 shows the antidune mobility number over time for the period when the lenses formed. *Fa* decreased abruptly around t = 2157 s and t = 2235 s, coinciding with the development of upstream-moving surface waves. It then oscillated before steadily decreasing after t = 2500 s, reaching the critical value around t = 2627 s, which is the same time as when the antidune over the lens began to move upstream (see Fig. 10). *Fa* continued decreasing below 1, then started to grow slowly around t = 2750 s, approaching the critical value again at t = 4000 s. Thus, the upstream movement of the antidune—crucial for lens preservation—can be explained by the parameter *Fa* and is associated with a steady decrease in the wave number due to the antidune wavelength growth (see Fig. 9b, between t = 2400 s and t = 2800 s).

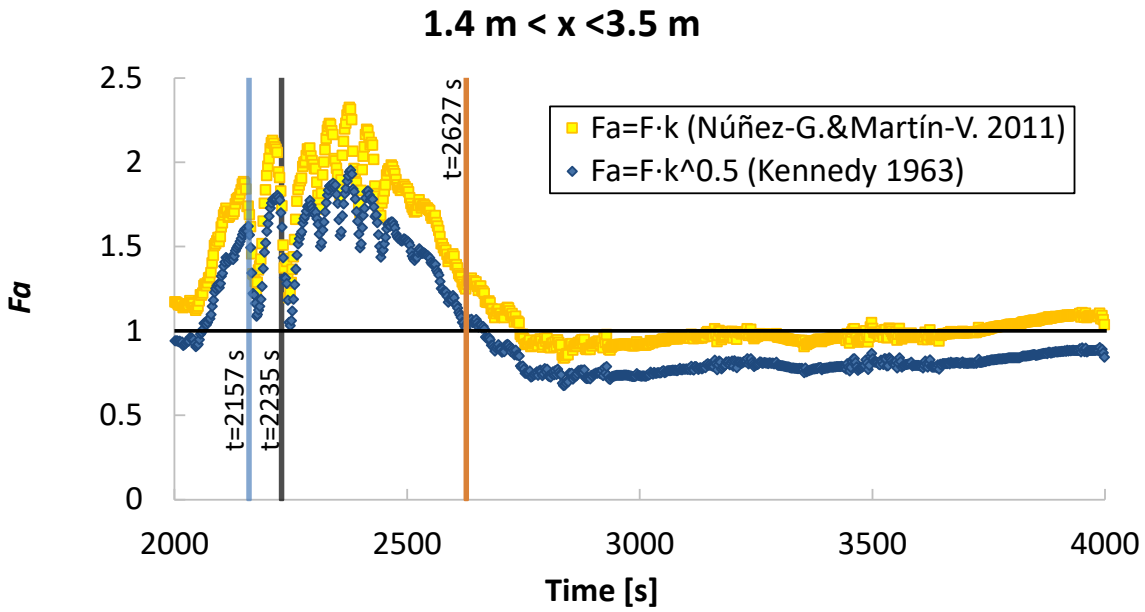

Figure 13. Temporal variation of the antidune mobility number F_a, computed with the characteristics of the dominant bedforms.

5. CONCLUSIONS

The numerical model was able to predict the formation of lenticular sedimentary structures using multiple sediment fractions in the bed. It also explained the hydraulic processes in detail, including velocity distributions, turbulence, bed shear stress, sediment sorting, non-hydrostatic pressure and upstream/downstream movement of the water surface waves and the antidune bed. In the current case, the lenticular structure was formed by an irregularity in the upstream boundary condition, lowering the water surface. This decreased the force from the non-hydrostatic pressure upstream of the antidunes causing an upstream-migrating water wave to move further than it otherwise would have. An upstream shift in the location of the antidune followed, making space for a layered lenticular sedimentary structure. The sedimentary structure itself was formed by smaller bed waves moving on top of the antidune bed. Each bed wave deposited a layer of fine and coarse material, often eroding parts of the layers below. The lines from layers of similar grain size distribution forms the pattern that make up the sedimentary structure, both in the field and in the numerical model.

The formation process is in line with results from physical model tests and accepted theory from the science of sedimentology (Alexander et al., 2001; Cartigny et al., 2014)

REFERENCES

809 Alexander, J. & Fielding, C. (1997) Gravel antidunes in the tropical
810 Burdekin River, Queensland, Australia. *Sedimentology* 44, 327–337.
811 https://doi.org/10.1111/j.1365-3091.1997.tb01527.x.
812
813 Alexander, J., Bridge, J.S., Cheel, R.J. & Leclair, S.F. (2001) Bedforms
814 and associated sedimentary structures formed under supercritical water
815 flows over aggrading sand beds. *Sedimentology* 48, 133–152.
816 https://doi.org/10.1046/j.1365-3091.2001.00357.x.
817
818 Baas, J. H., Best, J. L. & Peakall, J. (2016) Predicting bedforms and
819 primary current stratification in cohesive mixtures of mud and sand, *J.*
820 *Geol. Soc*., 173, 12–45. https://doi.org/10.1144/jgs2015-024.
821
822 Booker, D.J., Sear, D.A. & Payne, A.J. (2001) Modelling three-dimensional
823 flow structures and patterns of boundary shear stress in a natural pool-
824 riffle sequence. *Earth Surface Processes and Landforms 26*, 553–576.
825 https://doi.org/10.1002/esp.210.
826
827 Bridge, J.S. & Best, J.L. (1997) Preservation of planar laminae due to
828 migration of low-relief bed waves over aggrading upper-stage plane beds:
829 comparison of experimental data with theory. *Geomorphology 44*, 253–
830 262. https://doi.org/10.1111/j.1365-3091.1997.tb01523.x.
831
832 Bucher, J., del Papa, C., Hernando, I.R. & Almada, G. (2024) Upper-flow-
833 regime deposits related to glacio-volcanic interactions in Patagonia:
834 Insights from the Pleistocene record in Southern Andes, Sedimentology,
835 71 2314-2334, https://doi.org/10.1111/sed.13216.
836
837 Campbell, C.V. (1967) Lamina, Laminaset, Bed and Bedset.
838 *Sedimentology 8*, 2–26. https://doi.org/10.1111/j.1365-
839 3091.1967.tb01301.x.
840
841 Cartigny, M.J.B., Ventra, D., Postma, G. & van den Berg, J.H. (2014)
842 Morphodynamics and sedimentary structures of bedforms under
843 supercritical-flow conditions: New insights from flume experiments.
844 *Sedimentology 61*, 712–748. https://doi.org/10.1111/sed.12076.
845
846 Collinson, J. & Mountney, N. (2019) *Sedimentary Structures*, 4th Ed. Terra
847 Publishing, 352 pp. ISBN: 978-1-78046602-6.
848
849 Engelund, F. & Hansen, E. (1967) *A monograph on sediment transport in*
850 *alluvial streams*, Teknisk Forlag, Copenhagen, Denmark, 62 pp.
851
852 Escauriaza, C. & Williams, M. (2024) Antidune simulations using
853 continuum-based models. *Earth Surface Processes and Landforms*, e6058.
854 Available from: https://doi.org/10.1002/esp.6058
855

Fielding, C. (2006) Upper flow regime sheets, lenses and scour fills: Extending the range of architectural elements for fluvial sediment bodies. *Sedimentary Geology 190*, 227–240. https://doi.org/10.1016/j.sedgeo.2006.05.009.

Frechen, J. (1971) *Siebengebirge am Rhein, Laacher Vulkangebiet, Maargebiet der Westeifel: Vulkanologisch-petrographische Exkursionen*, 2nd. ed., Gebr. Borntraeger, Berlin – Stuttgart, 195 pp. (in German) Giri, S. & Shimizu, Y. (2006) Numerical computation of sand dune migration with free surface flow. *Water Resources Research* **42**, W10422. https://doi.org/10.1029/2005WR004588.

Han, K., Sun. J., Lin, B., Huang, Z. & Shi, X. (2023) Large-scale modelling of highly braided and laterally confined reach of a sand-bed river, *Earth Surface Processes and Landforms*, **48**:1557-1572 https://doi.org/10.1002/esp.5568

Hovikoski, J., Mäkinen, J., Winsemann, J., Soini, S., Kajuutti, K., Hepburn, A. & Ojala, A.E.K. (2023) Upper-flow regime bedforms in a subglacial triangular-shaped landform (murtoo), Late Pleistocene, SW Finland: Implications for flow dynamics and sediment transport in (semi-) distributed subglacial meltwater drainage systems, *Sedimentary Geology*, **454** 106448 https://doi.org/10.1016/j.sedgeo.2023.106448

Kennedy, J.F. (1963) The mechanics of dunes and antidunes in erodible-bed channels. *Journal of Fluid Mechanics 16*, 521–544. https://doi.org/10.1017/S0022112063000975.

Kopmann, R. (2020) Numerical simulation of dune movements during a flood event in River Elbe, Germany. *River Flow 2020 Proceedings of the 10th Conference on Fluvial Hydraulics, 7–10 July, Delft, Netherlands,* p. 565–573. https://doi.org/10.1201/b22619-80.

Launder, B.E. & Spalding, D.B. (1974) The numerical computation of turbulent flows. *Computer Methods in Applied Mechanics and Engineering 3*, 269–289. https://doi.org/10.1016/0045-7825(74)90029-2.

Leclair, S.F. (2002) Preservation of cross-strata due to the migration of subaqueous dunes: An experimental investigation. *Sedimentology 49*, 1157–1180. https://doi.org/10.1046/j.1365-3091.2002.00482.x.

Lunt, I.A. & Bridge, J.S. (2007) Formation and preservation of open-framework gravel strata in unidirectional flows. *Sedimentology 54*, 71–87. https://doi.org/10.1111/j.1365-3091.2006.00829.x.

Nabi, M., De Vriend, H.J., Mosselman, E., Sloff, C.J. & Shimizu, Y. (2013) Detailed simulation of morphodynamics: 3. Ripples and dunes. *Water Resources Research 49*, 5930–5943. https://doi.org/10.1002/wrcr.20457.

Naqshband, S., van Duin, O., Ribberink, J. & Hulscher, S (2015) Modeling river dune development and dune transition to upper stage plane bed. *Earth Surface Processes and Landforms 41*, 323–335. https://doi.org/10.1002/esp.3789.

Núñez-González, F. (2012) *Bed load transport of sand-gravel mixtures with antidunes – flume experiments*. PhD thesis, Technical University of Catalunya, Barcelona, Spain.

Núñez-González, F., & Martín-Vide, J. P. (2010). Downstream-migrating antidunes in sand, gravel and sand-gravel mixtures. In *Proceedings of the International Conference on Fluvial Hydraulics, River Flow* (pp. 393-400)..

Núñez-González, F., & Martín-Vide, J. P. (2011). Analysis of antidune migration direction. *Journal of Geophysical Research: Earth Surface*, *116*(F2).

Núñez-González, F., Martín-Vide, J. P., & Olsen, N. R. B. (2020). A specific energy diagram for antidunes. In *River Flow 2020* (pp. 552-558). CRC Press.

Olsen, N.R.B. (2015) Four free surface algorithms for the 3D Navier-Stokes equations. *Journal of Hydroinformatics 17*, 845–856. https://doi.org/10.2166/hydro.2015.012.

Olsen, N.R.B. (2017a) Numerical modelling of downstream-migrating antidunes. *Earth Surface Processes and Landforms 42*, 2393–2401. https://doi.org/10.1002/esp.4193.

Olsen, N. R. B (2017b) *Numerical modelling and hydraulics*, The Norwegian University of Science and Technology, ISBN 82-7589-074-7 https://pvv.org/~nilsol/documents/flures6.pdf

Olsen, N. R. B (2021) 3D numerical modelling of braided channel formation, *Geomorphology*, **375**, 107528. https://doi.org/:10.1016/j.geomorph.2020.107528.

Olsen, N.R.B. (2022) Explaining the formation of sedimentary structures under antidunes using a 2D width-averaged numerical model, Norwegian Journal of Geology, Vol. 102, https://doi.org/10.17850/njg102-3-2.

Patankar, S. (1980) *Numerical Heat Transfer and Fluid Flow*. T. Francis & Taylor publishers, 197 pp.

Rodi, W. (1980) *Turbulence models and their application in hydraulics*, IAHR State-of-the-art monograph.

Ruether, N., Olsen, N.R.B. and Eilertsen, R. (2008) 3D modeling of flow and sediment transport over natural dunes. *River Flow 2008: Proceedings of the International Conference on Fluvial Hydraulics, 3–5 September, Cesme, Izmir, Turkey*, 1479–1485.

Schmincke, H-U, Fisher, R. V. and Waters, A. C. (1973) Antidune and chute and pool structures in the base surge deposits of the Laacher See area, Germany. *Sedimentology* **20(4)** 553-574. https://doi.org/10.1111/j.1365-3091.1973.tb01632.x.

Schwarzmeier, C., Rettinger, C., Kemmler, S., Plewinski, J., Núñez-González, F., Köstler, H., Rüde, U and Vowinckel, B. (2023) Particle-resolved simulation of antidunes in free-surface flows, Journal of Fluid Mechanics, 961 R1, https://doi.org/10.1017/jfm.2023.262.

Slootman, A., Vellinga, A.J., Moscariello, A. and Cartigny, M.J.B. (2021) The depositional signature of high-aggradation chute-and-pool bedforms: The build-and-fill structure, *Sedimentology* https://doi.org/10.1111/sed.12843.

Vellinga, AJ, Cartigny, MJB, Eggenhuisen, JT & Hansen, EWM (2018) Morphodynamics and depositional signature of low-aggradation cyclic steps: New insights from a depth-resolved numerical model. *Sedimentology 65*, 540–560. https://doi.org/10.1111/sed.12391.

Warmink, J.J., Dohmen-Janssen, M.C., Lansink, J., Naqshband, S., van Duin, O.J.M., Paarlberg, A.J., Termes, P. & Hulscher, S.J.M.H. (2014) Understanding river dune splitting trough flume experiments and analysis of a dune evolution model. *Earth Surface Processes and Landforms 39,* 1208–1220. https://doi.org/10.1002/esp.3529.

Willis, J. C. & Kennedy, J. F. (1978) Sediment transport in migrating bed forms, *Proc. Verification of Mathematical and Physical Models in hydraulic Engineering*, ASCE, College Park, Md., 551-560.

Xavier, P. L. A., Scherer, C. M. dos S., dos Reis, A. D., de Souze, E. G., Guadagnin, F. & Piñeiro, G. (2022) Supercritical fluvial styles and the shifting aridity in the early Triassic: The example of the Sanga do Cabral Formation, Parana Basin, Brazil. Journal of Sedimentary Research, 93, 972-1006, https://doi.org/10.2110/jsr.2022.063

Yokokawa, M., Hasegawa, K., Kanbayashi, S. & Endo, N. (2010) Formative conditions and sedimentary structures of sandy 3D antidunes:

An application of the gravel step-pool model to fine-grained sand in an experimental flume. *Earth Surface Processes and Landforms 35*, 1720–1729. https://doi.org/10.1002/esp.2069.

SUPPORTING ONLINE ONLY INFORMATION

For the review process, videos are located at the web page:
https://nilsol.folk.ntnu.no/cases/lens
The videos will be uploaded to the ESPL web pages after the review process.